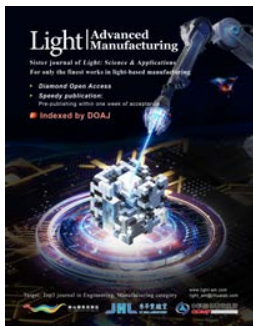**Accepted Article Preview: Published ahead of advance online publication**

Early Detection of Lithium Battery Leakage Using a Highly Sensitive in situ ZIF-8 Membrane-coated Micro-nano Optical Fibre

Shunfeng Sheng, Hao Li, Yi Zhang, Liangye Li, Kai Xiao, Xiukang Huang, Yunfei Liu, Wangyang Xu, Zhen Li, Lisong Yan, Zhijun Yan, Yunhui Huang, Qizhen Sun

Early Detection of Lithium Battery Leakage Using a Highly Sensitive in situ ZIF-8 Membrane-coated Micro-nano Optical Fibre

Shunfeng Sheng[1][†], Hao Li[1][†], Yi Zhang[2], Liangye Li[1], Kai Xiao[1], Xiukang Huang[1], Yunfei Liu[1], Wangyang Xu[1], Zhen Li[2], Lisong Yan[1], Zhijun Yan[1], Yunhui Huang[2], Qizhen Sun[1],[*]

[1] *School of Optical and Electronic Information, Huazhong University of Science and Technology, Wuhan, Hubei, 430074, China.*

[2] *State Key Laboratory of Material Processing and Die & Mould Technology, School of Materials Science and Engineering, Huazhong University of Science and Technology, Wuhan, Hubei, 430074, China.*

Author email addresses:

Shunfeng sheng: 19982905681@163.com; Hao Li: lhbeyond@hust.edu.cn; Yi Zhang: zhangyi2020@hust.edu.cn; Liangye Li: liangyeli@hust.edu.cn; Kai Xiao: kai_xiao@hust.edu.cn; Xiukang Huang: xiukang_huang@hust.edu.cn; Yunfei Liu: lyyf@hust.edu.cn; Wangyang Xu: M202272661@hust.edu.cn; Zhen Li: li_zhen@hust.edu.cn; Lisong Yan: yanlisong@hust.edu.cn; Zhijun Yan: yanzhijun@hust.edu.cn; Yunhui Huang: huangyh@hust.edu.cn;

* Corresponding author

Qizhen Sun

Email: qzsun@mail.hust.edu.cn

Telephone: 13667187589

Abstract

Detecting electrolyte leakage is an effective early warning approach for abnormal faults in lithium-ion batteries (LIB) and can help mitigate safety risks such as fires and explosions. However, detecting electrolyte leakage in the early stages of LIB faults presents a significant challenge, as leaks in LIBs produce volatile organic compounds (VOCs) at parts per million levels that are difficult to detect using conventional VOC sensors. Here, an effective LIB VOC sensor using micro-nano optical fibres (MNFs) has been developed for the first time, coated with an in situ

Early warning of lithium battery leakage

28 self-assembled zeolitic imidazolate framework-8 (ZIF-8) membrane as an electrolyte-sensitive layer.

29 The abundance of pores in ZIF-8 is excellent for adsorbing a variety of VOCs, including diethyl

30 carbonate, ethyl methyl carbonate, dimethyl carbonate, and propylene carbonate. The MNFs

31 possess high refractive index sensitivity, enhancing the online monitoring of electrolytes. MNFs

32 with a diameter of approximately 7 μm were assembled with four-cycle ZIF-8 of approximately 500

33 nm thickness, as the fabricated sensor. Through wavelength demodulation, the LIB sensor

34 demonstrated high sensitivity, detecting 43.6 pm/ppm of VOCs and exhibiting rapid response and

35 recovery times of typically within 10 min and 23 s, respectively, as well as a low theoretical

36 detection limit of 2.65 ppm for dimethyl carbonate vapor with excellent reversibility. The first

37 on-site verification of online LIB leakage monitoring demonstrated that the sensor achieved a 35 h

38 early warning prior to full-load leakage, thus exhibiting promising prospects for applications in

39 scenarios such as car batteries.

40 **Keywords**:   Lithium battery; Electrolyte leakage; Micro-nano optical fibres; Volatile organic

41 compounds; Zeolitic imidazolate framework-8; Dimethyl carbonate

Introduction

43 Lithium-ion batteries (LIB) have attracted considerable attention as a new energy technology and

44 have been widely used in energy storage systems, dominating the portable electronic products and

45 electric vehicles markets[1–3]. However, in most applications, external factors such as pressure,

46 vibration, temperature, overcharging, and discharging significantly impact the internal

47 electrochemical behaviour of LIBs and may cause potentially hazardous phenomena such as

48 thermal runaway (TR), which can lead to serious safety risks, including fire, explosion, or the

49 release of toxic gases[4,5]. To reduce safety risks and economic losses, implementing early screening

50 and warning strategies is essential for abnormal faults in LIBs.

51 Current LIB safety detection strategies entail monitoring parameters such as strain, temperature,

52 gas concentration, and electrical characteristics[6–9], playing crucial roles in detecting abnormal faults

53 at different stages of the LIB lifetime. However, thermocouples and voltage or current

54 measurements can only detect obvious battery failures when at least one cell is in a TR state.

55 Moreover, detecting a gas venting event that occurs prior to the TR state using thermocouples and

56 voltage measurements is challenging, because the working voltage remains stable, and the location

Early warning of lithium battery leakage

57 of the temperature increase is usually unknown[9]. On the other hand, gas sensors can detect battery

58 failures approximately 7–8 min prior to TR by monitoring gas emission, enabling earlier detection

59 of battery failure compared to temperature, voltage, and current measurements[10, 11].

60 Trace amounts of electrolyte vapour leakage can be considered an early symptom of LIB damage[9].

61 The electrolyte mixture used in LIBs typically contains volatile carbonate-based organic solvents

62 that can be detected using volatile organic compound (VOC) sensing technology, helping achieve

63 rapid and early warning of LIB failure at room temperature[5, 12]. VOC detection by gas

64 chromatography-mass spectrometry has high sensitivity and selectivity in the parts per trillion range;

65 however, its application is constrained by complex calibration operations and the need for off-site

66 testing[13]. To overcome these limitations, alternative VOC sensing technologies have been proposed,

67 such as quartz crystal microbalances[14], and electrochemical gas sensors[15], thermal conductivity gas

68 sensors[16], and metal oxide semiconductor gas sensors[17]. However, quartz-crystal microbalances are

69 not suitable for rapid detection despite their high sensitivity, electrochemical gas sensors are limited

70 by zero drift and aging, thermal conductivity gas sensors exhibit good operational stability but

71 suffer from low sensitivity and poor detection accuracy, and metal oxide semiconductor gas sensors

72 are easily influenced by environmental factors, such as high temperature and humidity. Overall, the

73 aforementioned techniques are limited by electromagnetic interference, extreme working

74 environments, and low sensitivity, rendering them unsuitable for in situ trace detection of VOCs

75 from LIBs.

76 In recent years, optical fibre sensors have emerged as promising candidates in the field of VOC

77 sensing due to minimal disturbance by environmental factors, and their compact size, high

78 sensitivity, and short response time. As a result, these advancements have garnered significant

79 attention and led to remarkable progress in the field[18–21]. Among these, external interferometers,

80 such as the Mach-Zehnder interferometer (MZI), possess long interference arms that provide high

81 sensitivity; however, they require complex demodulation methods and devices, making them large

82 and expensive[22]. Moreover, the Fabry-Pérot interferometer is insensitive to the refractive index (RI)

83 of reflecting surfaces and is unstable due to changes in cavity length caused by various

84 disturbances[23]. Various specialty optical fibres sense changes in RI induced by the interaction of

85 light with matter. However, the vast majority do not generate a sufficiently strong evanescent field[24,

86 25], which limits sensitivity. Notably, MNF have a waist region diameter on the micro/nano scale,

87 making them compact and facilitating both the coupling of external disturbances into the ultra-high

3

88   evanescent field and the decoupling of disturbances through wavelength or intensity demodulation

89   methods. Compared with other optical sensors, MNFs can detect the RI of the external environment

90   with ultrahigh sensitivity owing to their high evanescent field[22, 26–28]. In summary, considering the

91   need for simple demodulation methods, high sensitivity, and low disturbance requirements for VOC

92   sensing, MNFs are the most appropriate choice.

93   Despite their advantages, detecting trace amounts of VOCs poses a challenge for MNFs due to

94   the weak modulation of the RI of air near the surface of the VOC sensor at ppm concentrations.

95   Hence, VOC adsorbent materials are necessary as gas-sensitive layers to increase the VOC

96   concentration on the sensor surface by several orders of magnitude. Typically, MNFs are

97   functionalized to enhance their ability to detect specific substances. However, functionalized

98   materials rely on weak van der Waals forces to interact with MNFs, which renders the materials on

99   the fibre unstable owing to their small surface area and thickness. This instability leads to an

100   uncontrollable and unpredictable final optical spectrum, making them unsuitable for stable

101   measurements of LIBs[29, 30]. Improving functionalization methods is necessary to enhance gas

102   detection sensitivity. To date, a range of VOC sensitive materials have been reported, such as

103   organic polymers[31], carbon nanotubes[32], zeolites[33], metal oxides[34], and metal–organic frameworks

104   (MOFs)[35]. Among these materials, zeolitic imidazolate framework-8 (ZIF-8) exhibits exceptional

105   adsorptivity for VOC gas molecules due to its porous properties. Furthermore, ZIF-8 can

106   functionalize MNFs via in situ self-assembly through the formation of strong chemical bonds. Thus,

107   ZIF-8 is a promising candidate for VOC adsorption and offers a potential solution for increasing the

108   effective RI of the sensitive surface layer of MNFs[36].

109   In this study, a high-sensitivity LIB sensor has been proposed and demonstrated to warn LIB

110   faults at an early stage of electrolyte leakage through VOC sensing. The sensor utilizes MNFs as the

111   substrate, onto which a controlled, in situ self-assembled ZIF-8 membrane was deployed as the

112   sensitive layer; the proposed sensor is referred to as MNFs*ZIF. The performance of MNFs *ZIF

113   under various concentrations of LIB electrolyte components was measured and calibrated with high

114   sensitivity and fast response time through wavelength demodulation. In addition, MNFs*ZIF was

115   employed for online leakage monitoring of LIBs under working conditions for the first time,

116   providing early warning prior to the load ceasing. The proposed LIB sensor can provide high

117   sensitivity and stable detection of VOCs, as well as a fast response to LIB electrolyte leakage,

Early warning of lithium battery leakage

118 illustrating its potential application in the early warning of faulty LIBs in various commercial

119 products, such as electric cars.

Concept and methodology

121
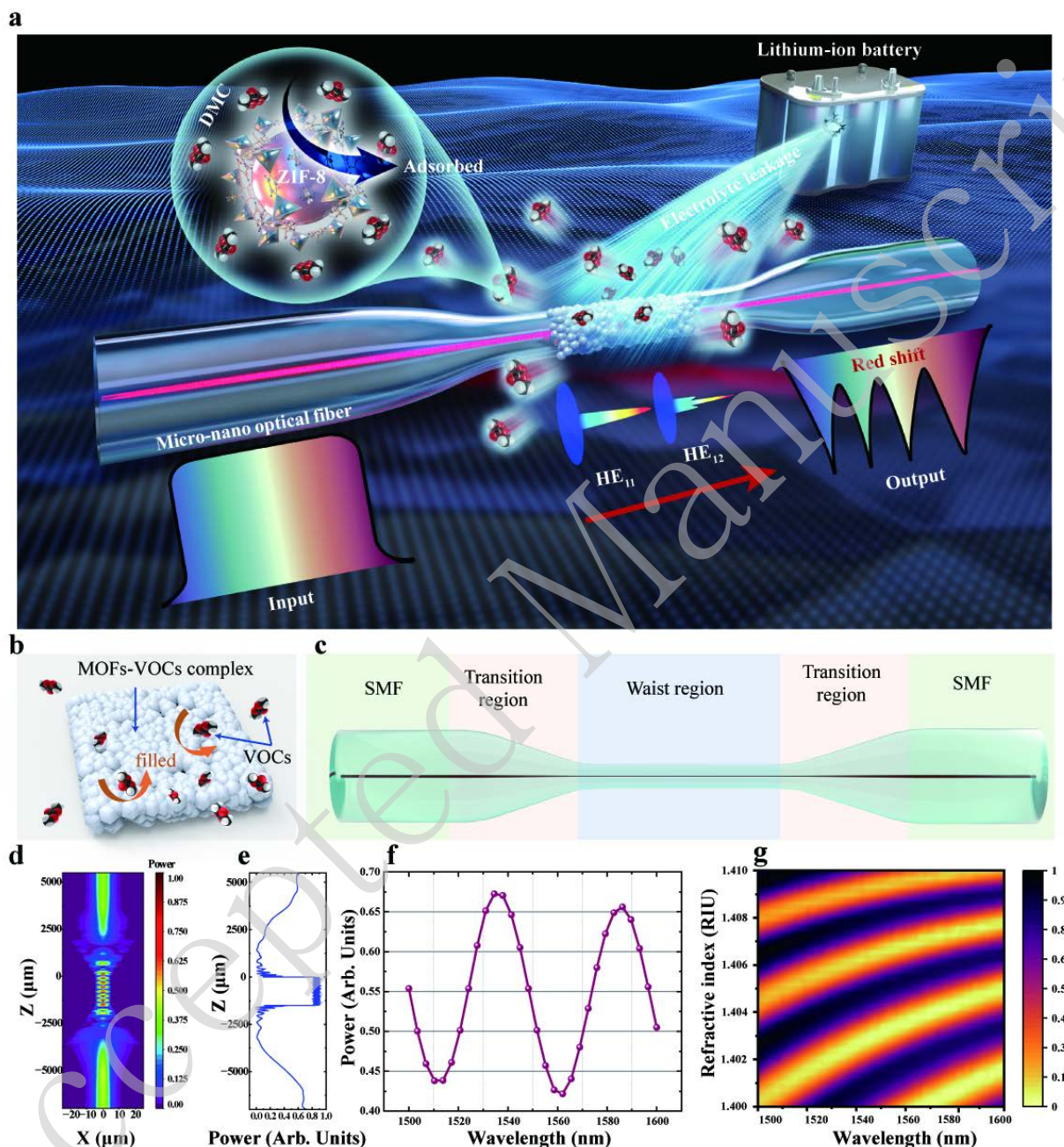
122 **Figure 1. Experimental concept and design principle.** LIB electrolyte vapour detection by MNFs*ZIF. **a,**
123 Concept of electrolyte detection in LIBs using ZIF-8 membrane-coated MNFs; small quantities of electrolyte
124 leaked from LIBs evaporates, generating gaseous DMC molecules, which causes a red-shift in the
125 transmission spectrum of DMC observed by MNFs*ZIF. **b,** Schematic of microporous MOFs filled with
126 VOCs to modulate the RI of the MOF-VOC complex. **c,** Typical structural diagram of MNFs, including
127 G.652 SMF, with the transition region featuring a steep taper assigned to the exciting HE_{12} mode, and the
128 waist region, several micrometers in diameter, where interference between HE_{12} and HE_{11} occurs. **d,** Intensity

5

129 contour map of light propagation along MNFs*ZIF, simulated using Rsoft, where the fundamental mode is
130 set as the launch light field, the monitored path represents the fibre core, and the output observing target
131 corresponds to the fibre base mode power in MNFs*ZIF, with the MNF modelled as an exponentially shaped
132 transition region. Light is confined to the fibre core in the SMF region, resulting in leakage of light power
133 into the cladding of the transition region. The modes of interference generate high-frequency power
134 oscillations in the waist region. **e,** Normalized power curve of the HE_{11} mode along the light propagation axis
135 of MNFs*ZIF under the fundamental mode light field input. **f,** Simulated transmission spectrum of
136 MNFs*ZIF from 1500 to 1600 nm with a wavelength sampling point of 30. **g,** Intensity contour map of the
137 MNFs*ZIF transmission spectrum from 1400 to 1600 nm with a wavelength sampling point of 60, and the
138 cladding RI ranging from 1.40–1.41 with a RI sampling point of 30.

139   The schematic diagram of the LIB leakage and ZIF-8 adsorption processes is shown in Fig. 1a.
140 The MNFs*ZIF was suspended on a bracket at the top of the chamber, together with the LIB cell
141 located at the bottom. Input and output optical signals were transmitted through single-mode optical
142 fibre (SMF) patch cords and flanges on the chamber. When the LIB fails, traces of electrolyte leak
143 and quickly evaporate into VOCs. A typical electrolyte vapor is dimethyl carbonate (DMC) vapor,
144 which migrates towards the top of the chamber and is adsorbed within theZIF-8 pores. The MNFs,
145 functioning as mode interference MZIs, are coated with an in situ self-assembled ZIF-8 membrane.
146 Given its large specific surface area and high porosity, DMC can be adsorbed by the ZIF-8
147 membrane, modulating the RI of the evanescent field in the MZI. DMC adsorption increases the
148 external RI of the MNFs, resulting in a red-shift in the transmission spectrum. Conversely,
149 desorption of VOCs induces a blue-shift, allowing for the determination of RI variation through
150 wavelength demodulation.

151   For optical VOC sensors, determining how the volume fraction of the target analyte in the MOF
152 film alters the effective RI of the MOF-VOC complex is crucial, as shown in Fig. 1b. This
153 relationship can be described by the following general equation for the RI of microporous substrates
154 filled with a fluid analyte[37]:

$$n = \sqrt{(V_{sub}n_{sub}^2 + V_a n_a^2 + (1 - V_{sub} - V_a)n_{vac}^2)} \tag{1}$$

155 where V_{sub} and V_a represent the volume fractions of the microporous substrate and fluid analyte,
156 respectively, and n_{sub}, n_a, n_{vac}, and n represent the RI indices of the microporous substrates, fluid
157 analyte, vacuum, and substrate-analyte complex, respectively. Given that the effective RI of the
158 ZIF-8 membrane without the analyte (n_{zif}) and filled with DMC vapour ($n_{dmc-zif}$) is known, the
159 volume fraction of DMC vapour in the ZIF-8 substrates (V_{DMC}) can be expressed by a simplified
160 equation:

Early warning of lithium battery leakage

$$V_{DMC} = (n_{dmc-zif}^2 - n_{zif}^2)\big/(n_{dmc}^2 - n_{vac}^2) \tag{2}$$

161   According to this relationship, the volume fraction of DMC vapour in the ZIF-8 substrate

162   increases as DMC vapour is adsorbed by the ZIF-8 membrane, which macroscopically manifests as

163   an increase in the effective RI of the ZIF-8 membrane[37]. A schematic of the MNF structure as

164   sensing carriers for LIB monitoring is depicted in Fig. 1c. When the HE_{11} fundamental mode in a

165   SMF is transmitted to tapered MNFs, the higher-mode HE_{12} is excited in the transition region and

166   leaks into the cladding. Subsequently, mode coupling occurs between HE_{11} and HE_{12}, allowing

167   them to propagate together along the waist region until the energy is recoupled back into the SMF

168   core through another symmetrical transition region, forming a mode interference MZI[38]. Due to the

169   dual-mode interference in MNFs, the wavelength demodulation method is utilised instead of

170   intensity demodulation, effectively improving sensing accuracy and detection range while avoiding

171   interference caused by light source fluctuations.

172   As the RI of the ZIF-8 membrane surrounding the MNFs changes, distinct changes in the

173   effective RIs of the two modes occur, resulting in a shift in the transmission spectrum that can be

174   demodulated using the wavelength demodulation method. The RI sensitivity of MNFs can be

175   characterised by the following relationship:

$$S = d\lambda_N\big/dn = (\lambda_N \frac{\partial(\Delta n_{eff})}{\partial n_{SRI}})\bigg/(\Delta n_{eff} - \lambda_N \frac{\partial(\Delta n_{eff})}{\partial \lambda_N}) \tag{3}$$

176   where $G = \Delta n_{eff} - \lambda_N\left(\partial(\Delta n_{eff})\big/\partial\lambda_N\right)$ is the group effective RI difference between the HE_{11} and

177   HE_{12} modes, representing the dispersion characteristics of the MNFs. Since the input wavelength is

178   approximately 1550 nm, the impact of variation in λ can be neglected. Therefore, the RI sensitivity

179   of MNFs is primarily determined by G, λ_N, and $\partial(\Delta n_{eff})\big/\partial\lambda_N$ [39].

180   To study the optical properties of the proposed MNFs*ZIF sensor, a simulation based on Rsoft

181   was conducted. A MNF with waist diameter of 7 μm was selected to balance sensitivity and

182   robustness. The thickness of the ZIF-8 membrane was set to 500 nm to optimize sensitivity while

183   minimizing extinction in the transmission spectrum. The RI of ZIF-8 was estimated to be 1.4,

184   according to previous reports[39].

185   The simulation results are displayed in Fig. 1d–g. The intensity of light propagation through the

186   MNF is shown in Fig. 1d, while Fig. 1e illustrates the optical power of the HE_{11} mode monitored

187   along the MNFs, revealing the power oscillation phenomenon caused by mode coupling in the waist
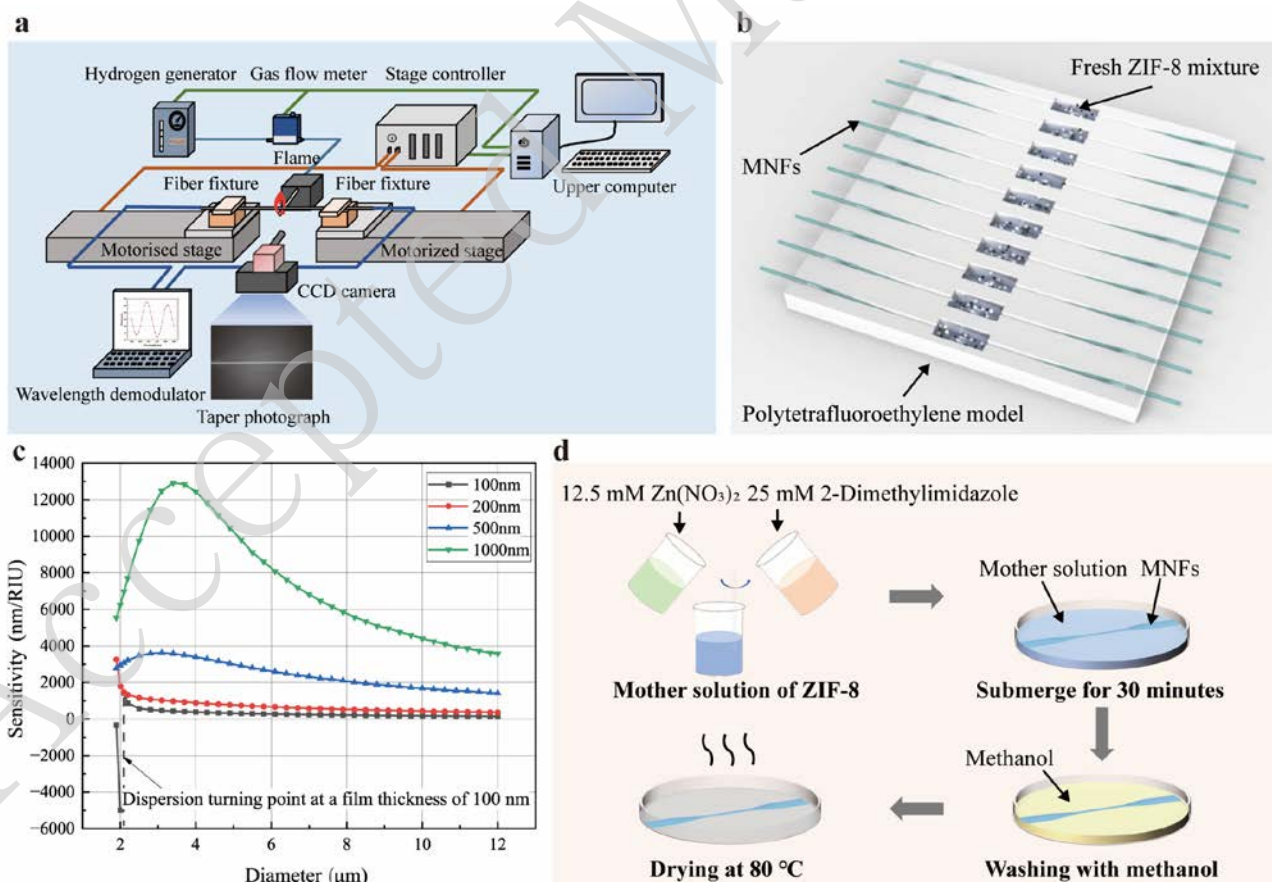
Early warning of lithium battery leakage

188 region. To obtain the theoretical transmission spectrum, the input wavelength was scanned from

189 1500 to 1600 nm, as shown in Fig. 1f. Assuming that the cladding material of the MNFs is ZIF-8

190 and that the RI variation of the cladding ZIF-8 is +0.1 RIU due to the adsorption of DMC vapor, the

191 results indicate a red-shift of several thousand nanometres, as depicted in Fig. 1g. This observation

192 confirms that the MNFs*ZIF sensor has an RI sensitivity of 24166.3 nm/RIU when the MNF

193 cladding material is a ZIF-8 membrane with a RI of 1.4. Therefore, the simulation results indicate

194 that the MNFs*ZIF sensor possesses ultrahigh theoretical RI sensitivity, capable of meeting the

195 requirements for detecting trace VOC concentrations.

196 **Fabrication and experimental methods**

197 **Fabrication of MNFs*ZIF**

198 MNFs were fabricated by rapidly drawing melted SMF using a hydrogen-oxygen flame. A

199 schematic of the MNF fabrication system is depicted in Fig. 2a. An MNF with a uniform waist

200 region diameter of 7 μm and a smooth surface was obtained using a hydrogen flow of 85 mL·min^{-1}

201 and a distance of 4.5 mm between both the motorized stages, with a drawing speed of 0.15 mm·s^{-1}.

202

203 **Figure 2. Methods for fabrication and ZIF-8 functionalization of the MNFs*ZIF sensor. a,** Schematic of

204 the MNF fabrication system. This system employs a wavelength demodulator to select the required

8

Early warning of lithium battery leakage

205 transmission spectrum, while a CCD camera ensures that the fiber remains aligned along the same axis
206 during the stretching process, facilitating real-time observation of the tapering process. **b,** Schematic of
207 ZIF-8 in-situ self-assembly on the MNFs within a polytetrafluoroethylene model. This model supports the
208 fabrication of up to 10 MNFs*ZIF from the same batch, with each solution container having a volume of 1.5
209 mL. The waist region of the MNFs is suspended and clamped in the model, where in-situ ZIF-8
210 self-assembly, cleaning with a methanol solution, and vacuum drying are performed to ensure the stability of
211 the adhered ZIF-8 on the MNF. **c,** Relationship between sensitivity, film thickness, and diameter; the selected
212 parameters for the MNFs*ZIF include a 7 μm diameter MNF modified with a 500 nm thick ZIF-8 film,
213 based on a comprehensive analysis of sensitivity enhancement and sensor robustness. **d,** Depiction of one in
214 situ ZIF-8 self-assembly cycle on the MNF substrate at room temperature; each step is conducted within the
215 model without transferring the MNFs, and the mother solution is mixed in a 1:1 volume ratio, with equal
216 amounts injected into each model container.

217 To enhance the sensitivity of the MNFs to DMC vapor, an in situ self-assembled ZIF-8
218 membrane was coated onto the MNFs. ZIF-8 offers several advantages, including high stability,
219 hydrophobicity, a highly regular pore structure, adjustable pore and cage sizes, and variable
220 flexibility. The specific parameters deployed included a pore size of 3.4 nm, cage diameter of 11.6
221 nm, specific surface area of 1730 $m^2 \cdot g^{-1}$, and pore volume of 0.63 $m^3 \cdot g^{-1}$. The materials used in this
222 process included zinc nitrate hexahydrate, 2-methylimidazole, methanol, and dimethyl carbonate,
223 all of which were of analytical purity and used without further purification. Given that the waist
224 diameter and evanescent field depth of the dual-mode interference MNFs were in the micrometer
225 range, the thickness of the ZIF-8 film was preferably set to the micrometer range or below. This
226 ensured efficient coupling between the change in RI of the ZIF-8 film and the evanescent field of
227 the MNFs, while also supporting stable growth of the film on the MNFs substrate. The in situ
228 self-assembly environment is illustrated in Fig. 2b, where the MNFs were fixed in the groove of a
229 polytetrafluoroethylene model, keeping them straight and suspended to ensure that the waist region
230 of the MNFs could be fully immersed in the central compartments for in situ self-assembly.

231 To analyse the optimised quantity and thickness of ZIF-8, a simulation was conducted using
232 Comsol, setting the RI of ZIF-8 at 1.4. The MNF RI sensitivity was modified using ZIF-8 films
233 with thicknesses of 100 nm, 200 nm, 500 nm, and 1 μm. As illustrated in Fig. 2c, although reducing
234 the diameter of the MNFs can improve sensitivity, the diameter should not be too small to ensure
235 the robustness of the sensor and fabrication success rate. In addition, a thicker ZIF-8 film resulted in
236 increased responsiveness of the sensor but led to greater loss of the HE_{12} mode, decreasing the
237 extinction ratio of the transmission spectrum. Therefore, after considering factors such as robustness,
238 sensitivity, accuracy, and fabrication success rate, the optimal configuration was determined to be a

9

Early warning of lithium battery leakage

239   500 nm-thick ZIF-8 film modified onto 7 μm diameter MNFs, achieving a sufficiently high RI

240   sensitivity of 2326 nm/RIU.

241   ZIF-8 films were grown in situ on the surface of MNFs through intermolecular hydrogen bonding

242   interactions, affording stable gas-sensing materials. By optimising the crystallisation process, dense

243   and highly crystalline ZIF-8 thin films were successfully generated on the MNFs. The in situ ZIF-8

244   self-assembly process is illustrated in Fig. 2d and can be described through the following steps:

245   First, a 20 mL methanol solution containing 12.5 mM zinc nitrate hexahydrate was mixed with

246   another 20 mL methanol solution containing 25 mM 2-methylimidazole and stirred at room

247   temperature. The freshly prepared mixture was then transferred to containers, and the MNFs were

248   submerged in the solution. After 30 min, the MNFs were thoroughly washed thrice with methanol

249   and dried. This sequence of steps constitutes one in situ self-assembly cycle. Following four cycles

250   of this process, the modified MNFs were dried in a vacuum oven at 80 °C overnight to yield the

251   LIB sensor[40]. Due to the columnar molecular structure of ZIF-8, the material exhibits a greater

252   capacity for adsorption compared to similar chain molecules[41], indicating that the van der Waals

253   forces between the VOCs from batteries and ZIF-8, along with the hydrogen bond acceptors

254   capable of generating strong hydrogen bonds with ZIF-8, are relatively strong. However, cyclic gas

255   molecules such as toluene face challenges in entering the ZIF-8 pores because of their larger

256   molecular cross-sectional area. Smaller molecules, such as hydrogen, present a minor difference in

257   RI compared to air, resulting in a low response in wavelength shift. In addition, non-polar

258   molecules in the atmosphere, such as nitrogen and oxygen, lack entities capable of hydrogen

259   bonding, leading to only weak interactions with ZIF-8. Consequently, sensors designed with this

260   material demonstrate excellent selectivity and are largely immune to interference from other volatile

261   compounds, including hydrogen, toluene, and nitrogen.

262   **Monitoring in situ self-assembly**

263   To further analyse the in situ self-assembled ZIF-8 membrane on the MNFs and verify the

264   effective crystallisation in the waist region of the MNFs, the evolution of the transmission spectrum

265   during the first three crystallisation cycles was monitored, as illustrated in Fig. 3. The results

266   indicate that the extinction ratio of the transmission spectrum of MNFs decreases with an increasing

267   number of crystallisation cycles, as shown in Fig. 3a–c. This decrease is attributed to the increase in

268   optical loss of the HE_{12} mode, which occurs with the increasing thickness of the ZIF-8 membrane,

269   leading to a greater power difference between the HE_{11} and HE_{12} modes. Additionally, the data

10

Early warning of lithium battery leakage

270 reveal that the first crystallization cycle induced only a minor red-shift of 7.42 nm in the

271 transmission spectrum. In contrast, the second and third growth cycles resulted in significant

272 red-shifts of 47.34 nm and 40.18 nm, respectively, as depicted in Fig. 3d–e. These observations

273 suggest that ZIF-8 underwent nucleation during the first crystallization cycle, forming a seed layer

274 characterized by a slow growth rate. In subsequent cycles, particularly during the second and third

275 cycles, the growth process accelerated, especially within the first 5 min. This monitoring of the

276 transmission spectrum provides valuable information regarding crystal growth, thereby facilitating

277 the controlled manufacturing of MNFs*ZIF sensors.
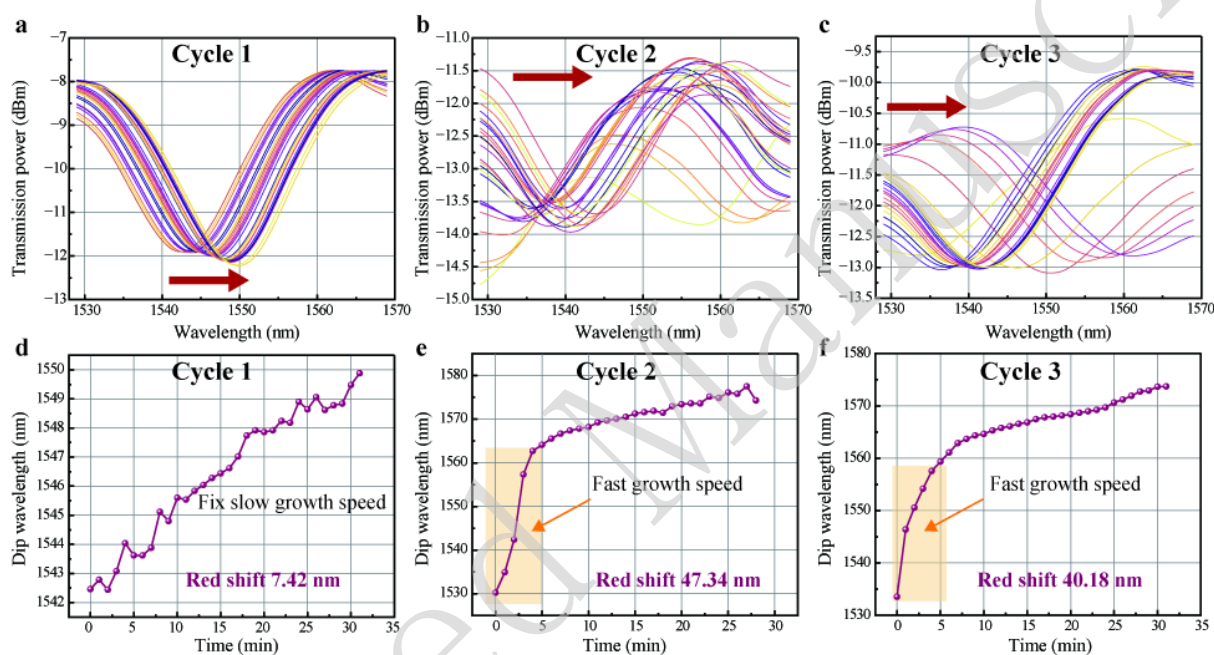
278

279 **Figure 3. In situ self-assembly process for ZIF-8 monitored by the transmission spectra of the MNFs**
280 **during the first three growth cycles.** The ZIF-8 was self-assembled in situ on the surface of bare MNFs
281 layer by layer, with the transmission spectrum of the MNFs at a frequency of 1 min over approximately 30
282 min. **a,** Evolution of the red-shift in the transmission spectrum recorded during the first growth cycle, with
283 measurements taken after 32 min. **b,** Evolution of the red-shift in the transmission spectrum recorded during
284 the second growth cycle, with measurements taken after 29 min. **c,** Evolution of the red-shift in the
285 transmission spectrum recorded during the third growth cycle, with measurements taken after 32 min. **d,**
286 Curve of dip wavelength position during the first cycle of ZIF-8 growth, tracking the dip observed at
287 approximately 1542 nm. **e,** Curve of peak wavelength position during the second cycle of ZIF-8 growth,
288 tracking the dip at approximately 1530 nm. **f,** Curve of peak wavelength position during the third cycle of
289 ZIF-8 growth, tracking the dip at approximately 1532 nm.

290 **Morphological characterization**

291 To analyse the crystallisation conditions for ZIF-8 on the surface of the MNFs, the ZIF-8

292 membranes were morphologically characterised before and after 1–4 cycles of in situ self-assembly,

293 as depicted in Fig. 4. The waist region diameter of the bare MNFs was approximately 7 μm,

11

Early warning of lithium battery leakage

294 exhibiting a smooth and uniform surface, as shown in the inset of Fig. 4a. Moreover, the size of the

295 ZIF-8 crystals increased with the number of self-assembly cycles, resulting in a denser and more

296 uniform ZIF-8 memberane. After four cycles of in situ self-assembly on bare MNFs, a ZIF-8

297 membrane with a thickness of 506 nm was achieved, as illustrated in Fig. S2, which aligns with the

298 simulated value of ZIF-8 membrane thickness. Collectively, the SEM images show that ZIF-8

299 crystals were grown with regular particle morphologies, resulting in tight and thick membranes.
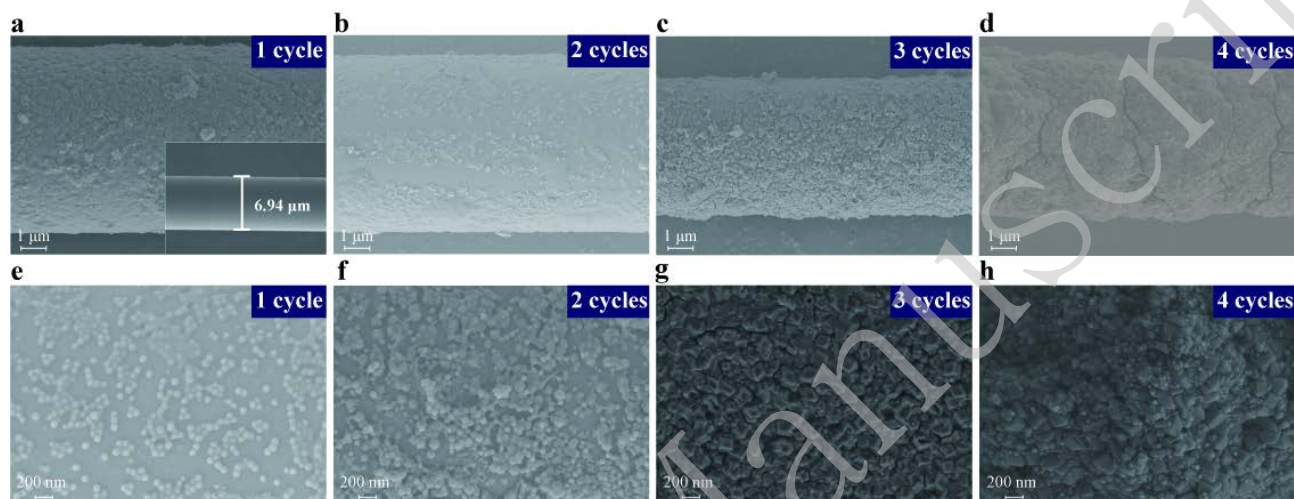
300

301 **Figure 4. SEM images of ZIF-8 membranes on MNFs following 1–4 self-assembly growth cycles.** The
302 SEM images were obtained at 3 kV extra high tension. **a,** SEM image after 1 cycle of in situ ZIF-8
303 membrane self-assembly on MNFs with a magnification of 9 k; the inset shows the SEM image of bare MNF
304 with a diameter of 6.94 μm. **b–d,** SEM images of MNFs after 1 to 4 cycles of in situ ZIF-8 membrane
305 self-assembly, all with a magnification of 9 k. **e–h,** Higher magnification SEM images of in situ ZIF-8
306 membranes self-assembled on MNFs: **e,** 1 cycle at 30,000×, **f,** 2 cycles at 20,000×, **g,** 3 cycles at 30,000×,
307 and **h,** 4 cycles at 30,000×.

308 **Experimental setup**

309 A schematic diagram of the wavelength demodulation sensing system for LIB electrolyte vapour

310 detection is shown in Fig. 5a. The system primarily consisted of a gas chamber, wavelength

311 demodulator, and fibre optic link. The fabricated MNFs*ZIF sensor was placed within a sealed

312 metal gas chamber with a 3 L volume (100 mm × 100 mm × 300 mm), equipped with a spherical

313 valve at the top for liquid introduction. The sensor was linked to a wavelength demodulator via two

314 SMF patch cords to acquire and monitor the transmission spectrum. The wavelength demodulator

315 recorded the transmission spectrum at intervals of 1 s or 1 min, over an acquisition range of 1530–

316 1570 nm in the C-band. A 10 μL pipette gun was used to inject DMC solvent into the chamber,

317 allowing the vaporized gas molecules to diffuse into the ZIF-8 membrane. The shift in the dip of

318 specific interference patterns within the transmission spectrum was tracked to quantify the

319 concentration of evaporated DMC.

12

Early warning of lithium battery leakage

320   Since the target analyte was injected as a liquid, the gas concentrations after evaporation required

321   conversion. According to the ideal gas law, under the conditions of 25 ℃ and standard atmospheric

322   pressure, the conversion between the volume of DMC solvent (V_{lq}) and volume concentration of

323   vapor (ρ_{vol}) in the gas chamber can be expressed as:

$$\rho_{vol} = \left(\rho_{lq} \times V_{lq} \times V_0 \times T\right)\big/\left(M \times T_0 \times V_{cham}\right)$$

324   (4)

325   Here $\rho_{lq} = 1.07\,g \cdot cm-3$ represents the DMC solvent density, $V_0 = 22.4\,L \cdot mol-1$ is the standard

326   molar volume of gas, $T_0 = 273\,K\ \left(T = 298\,K\right)$ is the temperature, $M = 90.078\,g \cdot mol-1$

327   represents the molar mass of DMC, and $V_{cham} = 3\,L$ is the volume of the chamber. Using this

328   relationship, the volume fraction of DMC vapor after the complete evaporation of 1 μL of the DMC

329   solvent in the gas chamber was calculated to be 96.82 ppm, as shown in Fig. 5b.
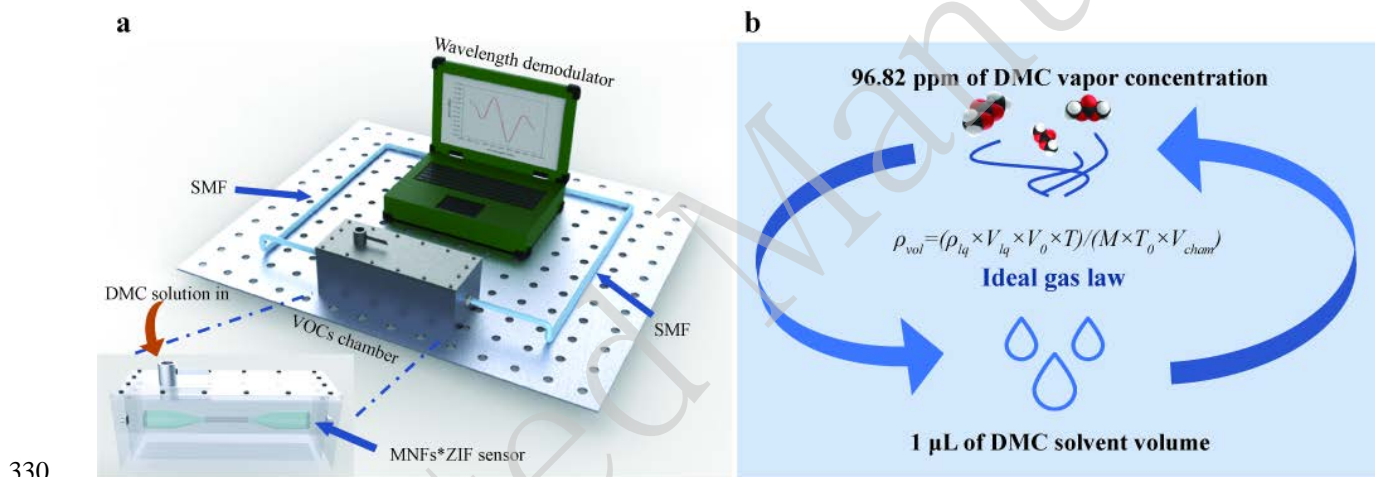
330

331   **Figure 5. Experimental setup for detecting LIB electrolyte vapor concentration. a,** Schematic diagram
332   of the MNFs*ZIF wavelength demodulation system, including the MNFs*ZIF sensor, VOC detection
333   chamber, wavelength demodulator, and SMF patch cables. The wavelength demodulator featured an
334   integrated light source, Bragg grating, photo detector, acquisition card, upper computer, and signal
335   processing algorithms. The MNFs*ZIF sensor was positioned at the top of the gas chamber to ensure
336   complete adsorption of evaporated solvent molecules. Silicone-sealed holes maintained the chamber's
337   airtightness, and a ball valve at the top allowed for rapid electrolyte injection. **b,** Schematic illustrating the
338   conversion between volume of the LIB electrolyte solvent and the resulting vapor concentration.

Results and discussion

339

Sensing performance for electrolyte vapor

340

341   To measure and calibrate the performance of the MNFs*ZIF sensor in detecting LIB electrolyte

342   vapor, DMC, the most common electrolyte solvent in batteries, was chosen as the test analyte.

343   Sequential injections of DMC solution (ranging from 0.2 to 4.5 μL) were administered into the gas

Early warning of lithium battery leakage

344   chamber using a pipette gun. These volumes corresponded to vapor concentrations between 19.4

345   and 435.7 ppm after full evaporation. The detection process was segmented into three phases:

346   evaporation, stabilization, and exhaust, during which the transmission spectrum of the sensor was

347   recorded at regular intervals. The detection outcomes are presented in Fig. 6.

348
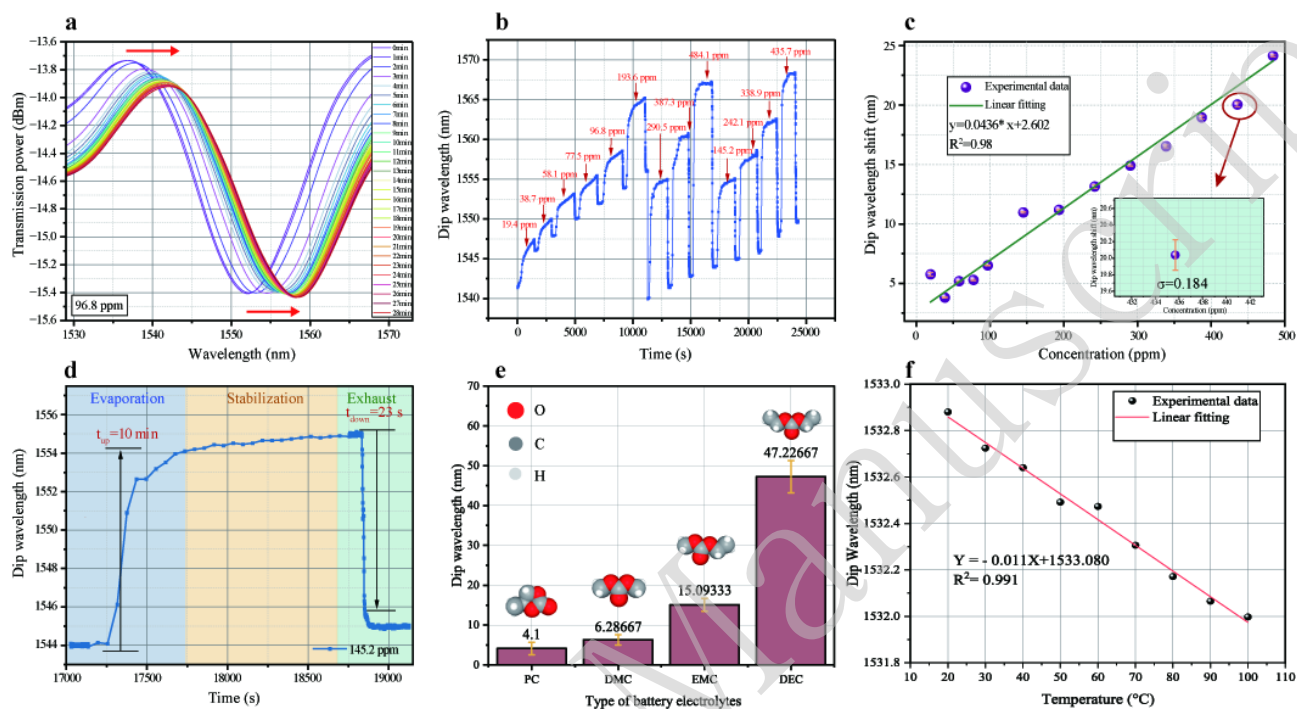
349   **Figure 6. Performance of MNFs*ZIF in detecting LIB electrolyte vapor. a,** Evolution of the red-shift in

350   the transmission spectrum of MNFs*ZIF over 28 min for a DMC vapor concentration of 96.8. **b,** Changes in

351   the dip wavelength position in the transmission spectrum across time for DMC concentrations ranging from

352   19.4 to 435.7 ppm, showing 13 distinct concentrations. The sensor's response phases include evaporation,

353   stabilization, and exhaust. **c,** Linear fit of MNFs*ZIF sensor response to DMC concentrations between 19.4

354   to 435.7 ppm, with error bars representing the standard deviation between pre- and post-adsorption

355   stabilization phases. **d,** Example of response and recovery time for the MNFs*ZIF sensor to DMC vapor at

356   145.2 ppm concentration. **e,** Resonant wavelength responses of MNFs*ZIF under 1 μL volumes of various

357   electrolyte compositions, including PC, DMC, EMC, and DEC, along with their chemical structures. **f,**

358   Temperature sensitivity of MNFs*ZIF measured over a range of 20–100 ℃ in 10 ℃/3-5minincrements,

359   controlled by a thermoelectric cooler.

360   The transmission spectrum varied with DMC evaporation time, showing a typical red-shift as the

361   evaporated DMC concentration increased from 19.4 to 193.6 ppm (Fig. 6a). In Fig. 6b, the

362   interference dip wavelength consistently shifted to longer wavelengths, indicating good reversibility

363   of the MNFs*ZIF sensor. After the sensor returned to its initial state, DMC concentration was

364   incrementally raised from 290.46 to 484.1 ppm, maintaining consistent sensor reversibility.

365   Repeated measurements at four concentrations (145.2 to 435.7 ppm) demonstrated repeatable

366   sensor behavior. Notably, a slight red-shift during the stable period followed each test cycle due to

367   minor instability in the wavelength demodulator's light source, which could be mitigated using

368 signal processing techniques like wavelet denoising. The sensor's functionality was restored after

369 each cycle by air exchange to remove residual gas molecules on the ZIF-8 surface. Linear fitting

370 yielded a sensitivity S of 43.6 pm/ppm for the 19.4–435.7 ppm range, with $R^2 = 0.98$ (Fig. 6c), with

371 accuracy influenced by pipette volume precision.

372   Key performance metrics for VOC detection include response time (t_{up}) and recovery time (t_{down}),

373 defined as the time to reach 90% of the maximum wavelength shift during evaporation and exhaust

374 phases, respectively. t_{up} depended on complete evaporation and diffusion of DMC into ZIF-8, while

375 t_{down} depended on desorption rate, yielding $t_{up} = 10$ min and $t_{down} = 23$ s at 145.2 ppm (Fig. 6d).

376 Notably, the response time of the MNFs*ZIF sensor was influenced by the relatively slow processes

377 of electrolyte evaporation and penetration into the membrane pores. Recovery, however, was rapid

378 due to the passive venting process, where DMC vapor exchanged directly with the atmosphere.

379 Active venting, such as nitrogen injection, was not used. The significant concentration gradient

380 facilitated swift DMC-air exchange, reducing the RI and causing a spectral blue-shift. The standard

381 deviation of noise during a 120 s stable state without the target material was denoted as σ, with a

382 typical value of 0.0385 nm. Moreover, the limit of detection (LOD) for the MNFs*ZIF sensor was

383 defined as 3σ/S, leading to a theoretical LOD of 2.65 ppm at a DMC concentration of 145.2 ppm.

384 With the wavelength demodulator resolution R set at 0.02 nm, the sensor's theoretical resolution R/S

385 was calculated to be 0.46 ppm, demonstrating the high sensitivity and low detection threshold of the

386 MNFsZIF sensor for DMC vapor.

387   To confirm the adsorption capabilities of MNFs*ZIF for LIB electrolytes, sensor responses to

388 four types of common electrolyte compositions was evaluated and compared, as shown in Fig. 6e.

389 Results indicated that the sensor was significantly more sensitive to diethyl carbonate (DEC) and

390 ethyl methyl carbonate (EMC) than to DMC and propylene carbonate (PC). The reduced response

391 to PC was attributed to its lower volatility relative to the other VOCs. Non-interference from other

392 volatiles, such as hydrogen, toluene, and oxygen, was confirmed based on the molecular adsorption

393 characteristics, including force, size, and polarity, analyzed during sensor fabrication. This selective

394 detection underscores the sensor's effectiveness, with the highest response observed for DEC. The

395 sensor's higher sensitivity to composite LIB electrolytes compared to single electrolytes like DMC

396 highlights its suitability for safety monitoring in battery leakage scenarios. Figure 6f illustrates the

397 sensor's temperature sensitivity, showing a minimal shift of –0.011 nm·°C⁻¹ over the 20–100 °C

398 range, which is negligible for gas detection applications.

15

Early warning of lithium battery leakage

399   In summary, the MNFs*ZIF sensor demonstrated exceptional sensitivity and resolution, with a

400   low detection limit and rapid response and recovery times for DMC vapor at ppm levels.

401   Performance comparisons with other VOCs sensor (Table S1) further emphasized its potential in

402   LIB leakage detection applications.

403   **Online LIB leakage monitoring**

404   To verify the capability of MNFs*ZIF for providing real-time early warnings of LIB leakage, an

405   experimental setup was created to simulate leakage from pouch lithium cells under working

406   conditions. The detection performance of MNFs*ZIF was compared to that of a light emitting diode

407   (LED) load to assess its effectiveness in identifying faults in defective batteries. The sensor and

408   battery were enclosed in an air-sealed chamber to prevent interference from other gases.

409   A pouch LIB cell containing DMC : DEC : EMC = 1:1:1 (*v/v*) electrolyte was placed in the

410   chamber, alongside the MNFs*ZIF sensor, with the LIB voltage monitored using a multimeter (Fig.

411   7a). First, the battery was tested under load to ensure it was functioning properly, powering the

412   LEDs with an initial voltage of 3.292 V. After 1 h, the battery voltage had dropped to 2.861 V,

413   marking the start of the monitoring phase. The voltage then continued to decrease at a consistent

414   rate as the LED consumed power from the LIB, as shown in Fig. 7b. To simulate a leakage event, a

415   puncture approximately 2 mm in diameter was made in the battery after 0.72 hours of monitoring

416   (Fig. 7a). Notably, this damage did not alter the rate at which the voltage decreased (Fig. 7b).

417
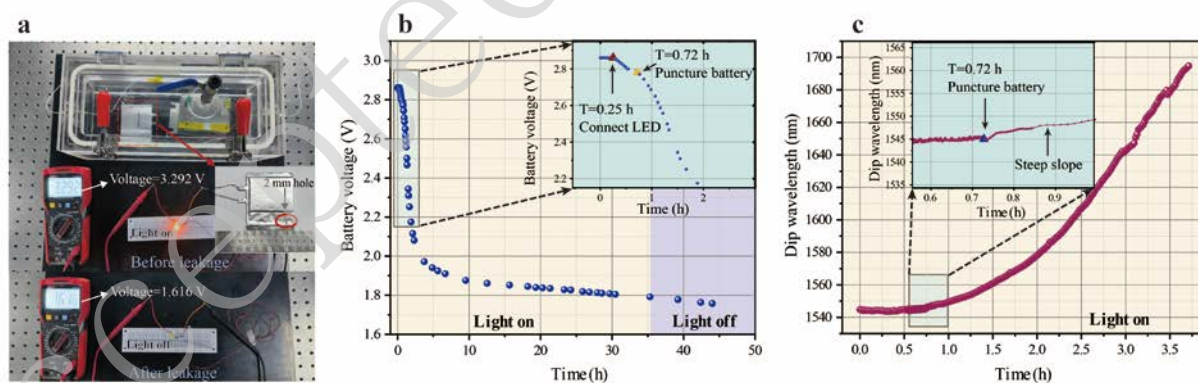
418   **Figure 7. Online leakage detection using the MNFs*ZIF sensor. a,** Diagram of the LIB electrolyte leakage

419   test system, where the MNFs*ZIF sensor was positioned at a high horizontal location in the chamber, and the

420   LIB was placed at the chamber's base. A pouch lithium cell with a nominal voltage of 3.65 V was punctured

421   with a hole approximately 2 mm in diameter to simulate leakage. An LED circuit, including a 100 Ω resistor

422   in series, completed the setup. The LIB's external voltage was continuously measured using a multimeter to

423   compare the voltage and LED status before (LED on, voltage = 3.939 V) and after (LED off, voltage = 1.616

424   V) the leakage event. **b,** Time-based variation of the LIB external voltage: at T < 0.25 h, the LIB remained

425   open; at T = 0.25 h, the LED was connected; at T = 0.72 h, the LIB was punctured, starting the leakage; at T

16

Early warning of lithium battery leakage

426 = 35 h, the LED was turned off. **c,** Changes in the MNFs*ZIF transmission spectrum's dip wavelength over
427 the first 3.5 h, recorded at 1-min intervals by the wavelength modulator, until saturation.

428   In contrast, the dip wavelength in the transmission spectrum of MNFs*ZIF showed an immediate
429 response to the leakage, characterized by a sudden steep slope (Fig. 7c), demonstrating the sensor's
430 capability to detect battery leakage with rapid response time. The dip wavelength underwent a
431 consistent red-shift of several hundred nanometers until saturation was achieved after 3.5 h,
432 effectively monitoring LIB leakage. Notably, even when the LIB voltage decreased to 2 V after this
433 period, the LED remained illuminated. The LIB voltage continued to decrease, reaching 1.616 V
434 until the leakage event occurred after 35 hours, at which point the LED load appeared to be off, as
435 illustrated in Fig. 7a. Overall, these results indicate that the MNFs*ZIF sensor is effective for online
436 monitoring of trace amounts of LIB electrolyte leakage and can provide early warnings of fault
437 events due to its high sensitivity, stability, rapid response time, immunity to other gases, and
438 robustness against temperature fluctuations.

Conclusions

440 In summary, a highly sensitive VOC sensor featuring in situ self-assembled ZIF-8 membrane-coated
441 MNFs has been fabricated for the early warning of online electrolyte leakage in LIB cells for the
442 first time. In our work, the detection principles of RI sensitivity in MNFs and the relationship
443 between the RI of the ZIF-8 membrane and VOC concentration was theoretically analysed.
444 Moreover, the MNFs*ZIF sensor was fabricated with a dense 500 nm thick in situ self-assembled
445 ZIF-8 membrane, which was grown in a controlled manner. To verify the performance of the
446 proposed MNFs*ZIF, gas concentration sensing experiments of DMC were carried out to calibrate
447 sensitivity, response time, and detection limit; the sensor achieved a sensitivity of 43.6 pm/ppm in
448 the ppm range for DMC vapour, as well as rapid response and recovery times averaging at 10
449 minutes and 23 seconds, respectively. The sensor also exhibited outstanding adsorption properties
450 for common electrolyte compositions over of other gases such as hydrogen and toluene.
451 Furthermore, a working-state LIB was monitored online by MNFs*ZIF, providing a red-shift of
452 hundreds of nanometres in the transmission spectrum and 35 h of early warning prior to the LED
453 load lights being switched off, demonstrating the excellent early warning capability of the
454 MNFs*ZIF. This study provides a highly sensitive, reversible, and fast response strategy for
455 promising energy and health diagnostics, with potential applications in electric cars, using in-situ
456 self-assembled ZIF-8 membrane-coated MNF sensors.

Early warning of lithium battery leakage

Acknowledgements

Author contributions

Q.S. conceived the project. S.S. and H.L. conceived the study and designed the experimental protocols. S.S. and Y.Z. jointly performed the experiments. L. L. and H. L. guided the fabrication process. X.K. and X.H. guided the characterisation process. S. S., Y. L., and W. X. conducted the theoretical analyses. Z. L., L. Y., Z. Y., and Y. H. contributed to the discussion of the results. Q.S. revised the manuscript accordingly.

Conflict of interests

The authors declare no competing interests.

†These authors contributed equally to this work.

Data availability

The data supporting the plots and other findings in this study are available from the corresponding authors upon reasonable request.

Supplementary information

Supplementary Information accompanies the manuscript on the Light: Advanced Manufacturing website (https://www.light-am.com/index.htm), and includes details of the transmission spectra of the MNFs after four growth cycle modifications (Fig. S1); an SEM image of the purified ZIF-8 powder (Fig. S2a); the thickness of the ZIF-8 membrane on the MNFs, as shown by SEM (Fig. S2b); a powder X-ray diffractogram of the ZIF-8 membrane on the MNFs (Fig. S2c); recyclability tests following 15 cycles (Fig. S3a); Bland-Altman error analysis of the 15-cycle recyclability tests (Fig. S3b); and a summary of VOC sensor performances over the last decade (Table. S1).

References

1. Ali, M. U. et al. Towards a smarter battery management system for electric vehicle applications: a critical review of lithium-ion battery state of charge estimation. *Energies* **12**, 446 (2019).

2. Zhang, X. H., et al. A review on thermal management of lithium-ion batteries for electric vehicles. *Energy* **238**, 121652 (2022).

487   3.   Zhang, H. L. et al. Recent progress in advanced electrode materials, separators and

488   electrolytes for lithium batteries. *Journal of Materials Chemistry A* **6**, 20564-20620 (2018).

489   4.   Essl, C. et al. Early detection of failing automotive batteries using gas sensors. *Batteries* **7**,

490   25 (2021).

491   5.   Wang, Q. S. et al. Progress of enhancing the safety of lithium ion battery from the

492   electrolyte aspect. *Nano Energy* **55**, 93-114 (2019).

493   6.   Li, Y. P. et al. Operando decoding of surface strain in anode-free lithium metal batteries via

494   optical fiber sensor. *Advanced Science* **9**, 2203247 (2022).

495   7.   Miao, Z. Y. et al. Direct optical fiber monitor on stress evolution of the sulfur-based

496   cathodes for lithium-sulfur batteries. *Energy & Environmental Science* **15**, 2029-2038

497   (2022).

498   8.   Zhang, Y. et al. Health monitoring by optical fiber sensing technology for rechargeable

499   batteries. *eScience* **4**, 100174 (2024) doi: 10.1016/j.esci.2023.100174.

500   9.   Dotoli, M. et al. A review of mechanical and chemical sensors for automotive li-ion battery

501   systems. *Sensors* **22**, 1763 (2022).

502   10.   Li, S. X. et al. Room temperature resistive hydrogen sensor for early safety warning of li-ion

503   batteries. *Chemosensors* **11**, 344 (2023).

504   11.   Wang, Z. et al. Gas sensing technology for the detection and early warning of battery

505   thermal runaway: A review. *Energy & Fuels* **36**, 6038-6057 (2022).

506   12.   Meng, X. N. et al. Ultrasensitive gas sensor based on Pd/SnS$_2$/SnO$_2$ nanocomposites for

507   rapid detection of H$_2$. *Sensors and   Actuators B*: Chemical **359**, 131612 (2022).

508   13.   Na, C J. et al. An efficient tool for the continuous monitoring on adsorption of sub-ppm

509   level gaseous benzene using an automated analytical system based on thermal

510   desorption-gas chromatography/mass spectrometry approach. *Environmental Research* **182**,

511   109024 (2020).

512   14.   Diltemiz, S. E. & Ecevit, K. High-performance formaldehyde adsorption on CuO/ZnO

513   composite nanofiber coated QCM sensors. *Journal of Alloys and Compounds* **783**, 608-616

514   (2019).

515   15.   Shirsat, M. D. et al. Polyaniline nanowires-gold nanoparticles hybrid network based

516   chemiresistive hydrogen sulfide sensor. *Applied Physics Letters* **94** 083502 (2009).

517   16.   Zhang, H. Q. et al. Research on a fast-response thermal conductivity sensor based on carbon

Early warning of lithium battery leakage

518   nanotube modification. *Sensors* **18**, 2191 (2018).

519   17.   Garzella, C. et al. TiO$_2$ thin films by a novel sol–gel processing for gas sensor applications.

520   *Sensors and Actuators B*: *Chemical* **68**, 189-196 (2000).

521   18.   Pathak, A. K. & Viphavakit, C. A review on all-optical fiber-based VOC sensors: heading

522   towards the development of promising technology. *Sensors and Actuators A*: *Physical* **338**,

523   113455 (2022).

524   19.   Wu, Y. et al. Graphene-coated microfiber Bragg grating for high-sensitivity gas sensing.

525   *Optics Letters* **39**, 1235-1237 (2014).

526   20.   Quan, M. R., Tian, J. J. & Yao, Y. Ultra-high sensitivity Fabry–Perot interferometer gas

527   refractive index fiber sensor based on photonic crystal fiber and Vernier effect. *Optics*

528   *Letters* **40**, 4891-4894 (2015).

529   21.   Lopez-Torres, D. et al. Comparison between different structures of suspended-core

530   microstructured optical fibers for volatiles sensing. *Sensors* **18**, 2523 (2018).

531   22.   Yang, L. Y. et al. Highly sensitive and miniature microfiber-based ultrasound sensor for

532   photoacoustic tomography. *Opto-Electronic Advances* **5**, 200076 (2022).

533   23.   Yang, L. Y. et al. Multi-channel parallel ultrasound detection based on a photothermal

534   tunable fiber optic sensor array. *Optics Letters* **47**, 3700-3703 (2022).

535   24.   Sun, Y. Z. et al. Theoretical and experimental analysis of the directional RI sensing property

536   of tilted fiber grating. *Journal of Lightwave Technology* **39**, 674-681 (2021).

537   25.   Sun, Y. Z. et al. Sensitivity adjustable biosensor based on graphene oxide coated excessively

538   tilted fiber grating. *Sensors and Actuators B*: *Chemical* **351**, 130832 (2022).

539   26.   Li, L. Y. et al. Wearable alignment-free microfiber-based sensor chip for precise vital signs

540   monitoring and cardiovascular assessment. *Advanced Fiber Materials* **4**, 475-486 (2022).

541   27.   Li, Y. P. et al. Immobilized optical fiber microprobe for selective and high sensitive glucose

542   detection. *Sensors and Actuators B*: *Chemical* **255**, 3004-3010 (2018).

543   28.   Li, L. Y. et al. Automatic and continuous blood pressure monitoring via an

544   optical-fiber-sensor-assisted smartwatch. *PhotoniX* **4**, 21 (2023).

545   29.   Yao, B. C. et al. Graphene enhanced evanescent field in microfiber multimode

546   interferometer for highly sensitive gas sensing. *Optics Express* **22**, 28154-28162 (2014).

547   30.   Yu, C. B. et al. Miniature fiber-optic NH$_3$ gas sensor based on Pt nanoparticle-incorporated

548   graphene oxide. *Sensors and Actuators B*: *Chemical* **244**, 107-113 (2017).

Early warning of lithium battery leakage

549   31.   Liu, H B., Yang, B. & Xue, N D. Enhanced adsorption of benzene vapor on granular
550   activated carbon under humid conditions due to shifts in hydrophobicity and total micropore
551   volume. *Journal of Hazardous Materials* **318**, 425-432 (2016).

552   32.   Pan, B. & Xing, B. S. Adsorption mechanisms of organic chemicals on carbon nanotubes.
553   *Environmental Science & Technology* **42**, 9005-9013 (2008).

554   33.   Ning, X. P. et al. Zeolite thin film-coated spherical end-face fiber sensors for detection of
555   trace organic vapors. *Optics Communications* **364**, 55-59 (2016).

556   34.   Liu, S. Q. et al. Novel sea urchin-like hollow core–shell SnO_2 superstructures: facile
557   synthesis and excellent ethanol sensing performance. *Sensors and Actuators B*: *Chemical*
558   **151**, 229-235 (2010).

559   35.   Campbell, M. G. et al. Chemiresistive sensor arrays from conductive 2D metal–organic
560   frameworks. *Journal of the American Chemical Society* **137**, 13780-13783 (2015).

561   36.   Ma, X. X. et al. On-chip integration of a metal–organic framework nanomaterial on a SiO_2
562   waveguide for sensitive VOC sensing. *Lab on a Chip* **21**, 3298-3306 (2021).

563   37.   Vandezande, W. et al. Parts per million detection of alcohol vapors via metal organic
564   framework functionalized surface plasmon resonance sensors. *Analytical Chemistry* **89**,
565   4480-4487 (2017).

566   38.   Ravets, S. et al. Intermodal energy transfer in a tapered optical fiber: optimizing
567   transmission. *Journal of the Optical Society of America A* **30**, 2361-2371 (2013).

568   39.   Huang, Y. et al. Ultrafast response optical microfiber interferometric VOC sensor based on
569   evanescent field interaction with ZIF-8/graphene oxide nanocoating. *Advanced Optical*
570   *Materials* **10**, 2101561 (2022).

571   40.   Hromadka, J. et al. Highly sensitive volatile organic compounds vapour measurements using
572   a long period grating optical fibre sensor coated with metal organic framework ZIF-8.
573   *Sensors and Actuators B*: *Chemical* **260**, 685-692 (2018).

574   41.   Luebbers, M. T., et al. Effects of molecular sieving and electrostatic enhancement in the
575   adsorption of organic compounds on the zeolitic imidazolate framework ZIF-8. *Langmuir* **26**,
576   15625-15633 (2010).